 DOI: 10.1109/JLT.2022.3158423

Multiband Silicon Photonic ePIC Coherent Receiver for 64 GBd QPSK

Pascal M. Seiler, Karsten Voigt, Anna Peczek, Galina Georgieva, Stefan Lischke, Andrea Malignaggi, and Lars Zimmermann

(Post-Deadline Paper)

***Abstract*—Multiband coherent communication is being handled as a promising candidate to address the increasing demand for higher data rates and capacity. At the same time, coherent communication is expected to enter the data center domain in the near future. With coherent data links in both, data- and telecom, spanning multiple optical bands, novel approaches to coherent transceiver design and traffic engineering will become a necessity. In this work, we present a monolithically integrated silicon photonic coherent receiver for O- and C-band. The receiver features a 2 × 2 multi-mode interference coupler network as 90° hybrid optimized for 1430 nm (E-band). The total power consumption is 460 mW at a footprint of approximately 6 mm^2, and an opto-electrical bandwidth of 33 GHz. 64 GBd operation is demonstrated in O- and C-band, which is competitive to the state-of-the-art for silicon photonic coherent receiver in the C-band, and the highest symbol rate to date for O-band coherent communication.**

***Index Terms*—coherent communication, silicon photonics, coherent receiver, multiband communication, O-band, C-band, dual window, BiCMOS**

I. Introduction

OPTICAL communication in the data- and telecom domain is the backbone of many modern day applications, like streaming, social media and cloud-computing. The importance of power- and cost efficient traffic engineering has recently been highlighted by the global COVID-19 pandemic. Remote working related applications, i.e. virtual private networks (VPN) and video conferencing, increased in traffic by more than 200% [1]. The rapid increase in demand for higher data rates has also lead to intense debates about the future deployment of coherent communication in data centers [2]–[6], blurring the line between long-haul and data center communication. Novel power- and cost efficient approaches to coherent data- and telecom links are therefore of utmost importance. Multiband approaches to coherent communication have been increasingly discussed as means for extending the use of legacy fiber, and operation over a 150 nm window from S- to L-band has been reported [7]. High-speed hybrid integrated lithium niobate ($LiNbO_3$) on silicon modulators for O- to C-band [8] have been demonstrated, rendering the entire optical domain from O- to C-band transparent to coherent communication. Noteworthy alternative approaches include the all-optical conversion from C- to O-band by nonlinear four-wave mixing in multi-mode silicon waveguides [9]. With the convergence of coherent links across optical bands spanning more than 300 nm, cost efficient multiband coherent receiver may become a necessity.

In this contribution, we extend our previous experimental work [10], in which we demonstrated the first silicon photonic dual window coherent receiver monolithically co-integrating high-speed electronics. We included a new section addressing the advantages of using a 2 × 2 multi-mode interference coupler (MMI) network as 90° hybrid in a multiband approach over conventional 4 × 4 or 2 × 4 MMIs commonly used in singleband coherent receivers [11], [12]. This also includes a more detailed analysis of the 2 × 2 MMI network through simulation results. We also present new experimental results, demonstrating 64 GBd quadrature-phase shift-keying (QPSK), which is an increase in symbol rate by a factor of two to the previous work on silicon photonic multiband coherent receiver [13]. Finally, we incorporated a section comparing the device in this work to other recently reported silicon photonic coherent receivers.

II. Receiver Design

The presented dual window coherent receiver was fabricated in IHP's 0.25 μm photonic BiCMOS technology, which monolithically integrates bulk-silicon high-speed radio frequency electronic- and 220 nm silicon-on-insulator photonic devices [14], [15]. A photograph of the fabricated device is shown in the top of Fig. 1a. The total footprint of the device is 3.61 mm × 1.66 mm (approximately 6 mm^2). Schematics of the optical- and electrical circuits are given in the bottom of Fig. 1a and in Fig. 1b, respectively.

P.M. Seiler, K. Voigt, and L. Zimmermann are with the Department of Silicon Photonics, Technische Universität Berlin, Berlin, Germany, and IHP - Leibniz-Institut für innovative Mikroelektronik, Frankfurt (Oder), Germany e-mail: seiler@tu-berlin.de.

A. Peczek is with IHP Solutions GmbH, Frankfurt (Oder), Germany.

G. Georgieva is with the Department of Radio-Frequency Technologies - Photonics, Technische Universität Berlin, Berlin, Germany.

S. Lischke and A. Malignaggi are with IHP - Leibniz-Institut für innovative Mikroelektronik, Frankfurt (Oder), Germany.

Manuscript received November 15, 2021.

This work was supported by the H2020-SPACE-ORIONAS project from the European Union's Horizon 2020 research and innovation program under grant agreement No. 822002. This is an own version of manuscript submitted to IEEE for publication. Posting of own manuscript version is permitted under IEEE sharing policies: https://www.ieee.org/publications/rights/index.html

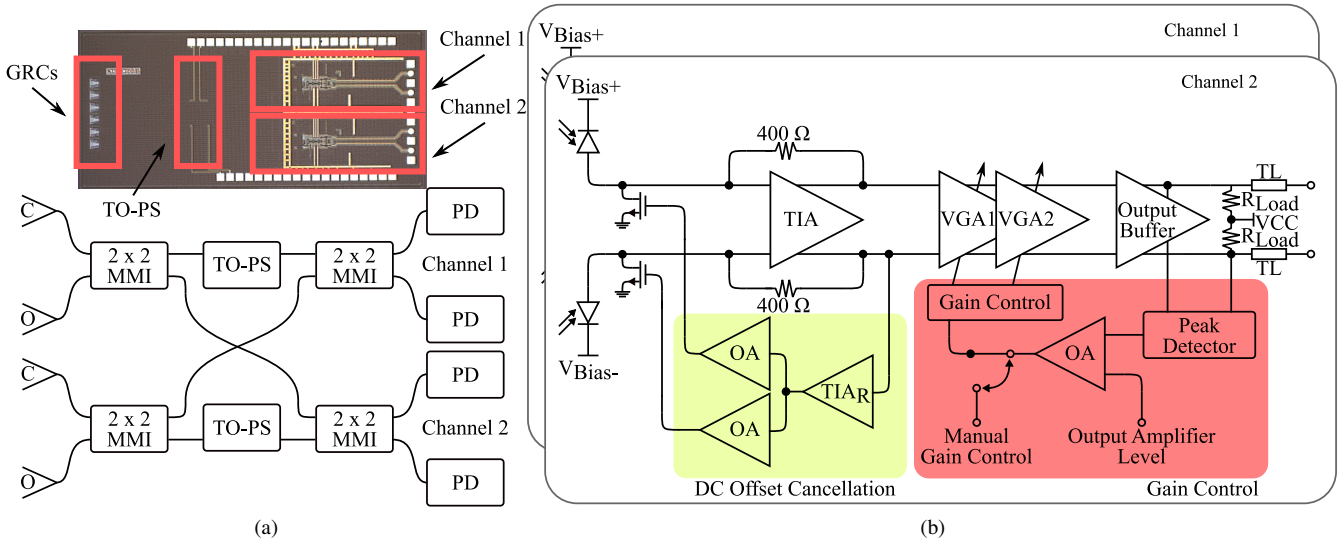

Fig. 1: Schematics of the dual window coherent receiver. a) top: photograph of the fabricated receiver. bottom: Optical section with GRC for either O- and C-band, a 2×2 MMI network acting as 90° hybrid, and photodiodes. b) Monolithically integrated electrical output section. GRC: grating coupler, MMI: multi-mode interference coupler, TO-PS: thermo-optic phase shifter, PD: photodiode, OA: operational amplifier, TIA: transimpedance amplifier, TIA_R: Replica TIA, VGA: variable gain amplifier, TL: transmission line, VPD: photodiode bias voltage.

A. *Optical Interface and 2 × 2 MMI Network*

On the optical side, 1-dimensional focusing grating couplers (GRC) are used as input. Instead of a conventional 4 × 4 MMI as 90° hybrid, a 2 × 2 MMI network [16], [17] is implemented. Due to the more complex MMI network, an additional phase shift of 90° is required for a proper separation of in-phase (I) and quadrature (Q) components, which is realized with thermo-optic phase shifters. Given the simultaneous operation on O- and C-band, the MMIs are designed with a central wavelength of 1430 nm. The geometry of the fabricated MMI is shown in Fig. 2a. It has a width of 10 μm at a length of 142.6 μm at a port spacing of 3.6 μm. Tapers with a length of 25 μm and have been used for access. Simulated results of the 2 × 2 MMI network for the differential imbalance and the normalized phase error are shown in Fig. 2b and Fig. 2c, respectively. The port enumeration is given as inset in Fig. 2b. From O- to C-band, the imbalance between output ports 1 and 2 (3 and 4) is below 1 dB, and reaches approximately 2 dB in the L-band. It needs to be noted, that there is additional imbalance between channel 1 and 2 due to the first MMI, which is not visible in Fig. 2b. The phase error is expressed as the output phase error relative to output port 1 and normalized to the ideal phase difference [17]. A compensation of the phase error originating from the first set of MMIs in Fig. 1b using the phase shifters is assumed. At 1310 nm and 1550 nm, the loss per MMI is below 2 dB.

The reasoning behind choosing a 2 × 2 MMI is two-fold. 1) The imbalance and phase error using a 4 × 4 MMI would quickly rise to impractical levels, while 2 × 2 MMIs offer a larger optical bandwidth [18]. 2) The phase error expressed by the first set of MMIs can be compensated with the phase shifters, without losing a proper IQ separation. Additionally, variable optical attenuators (VOA) can be easily implemented, compensating for the imbalance.

In this first prototype, GRCs have been chosen due to their reliability and the possibility of on-wafer testing. In future iterations, however, broadband optical interfaces suitable for communication from O- to L-band, i.e. spot-size converters (SSC), should be implemented. The additional use of polarization rotator-splitter would also allow for an efficient realization of dual polarization coherent receivers, avoiding concerns regarding the non-orthogonality of 2-dimensional GRCs [19]. The use of SSCs would not only improve the coupling efficiency, but also open the device to communication links from O- to L-band. Given the MMI design wavelength of 1430 nm, the device can be expected to show an improved performance in E- and S-band, when compared to O- and C-band. Finally, the MMI network is terminated by single-ended photodiodes [20].

Table I shows the expected on-chip loss at 1310 nm and 1550 nm. Optimized O-band GRC in this technology with approximately 1 dB improved coupling efficiencies in comparison to C-band GRCs have been demonstrated [6]. Note, that these values exclude an additional penalty for the back-end of line process. The total waveguide loss in both bands is approximately 0.3 dB. The largest loss contribution originates from the MMI network, which is separated in the inherent 6 dB lost per output port, and additional losses. The ± sign indicates the variation at the individual output ports, caused by the crossing shown in Fig. 1a and imbalances in Fig. 3. Adding all of these values gives the expected total power lost per output port of the 90° hybrid, being 12.6 ± 0.3 dB at 1310 nm and 12.8 ± 0.3 dB at 1550 nm.

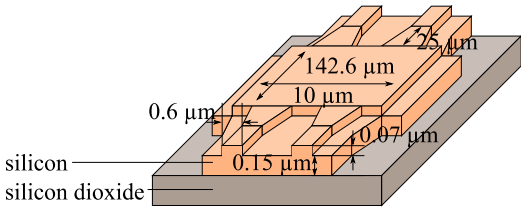

(a)

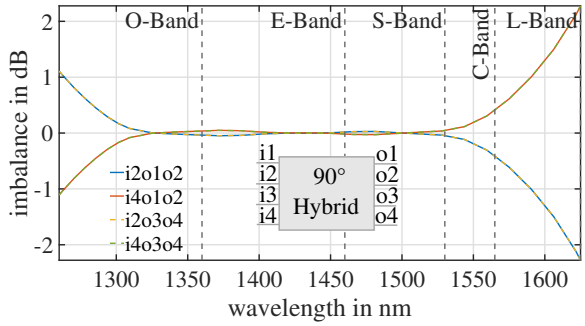

(b)

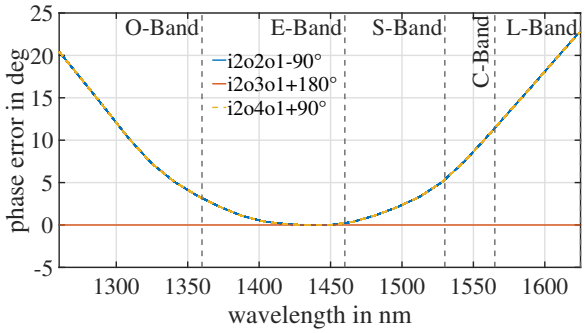

(c)

Fig. 2: Simulated 90° hybrid performance. (a) MMI geometry. (b) Differential imbalance with the port enumeration as inset. (c) Phase error relative to output port 1, normalized to the ideal phase difference. The phase error of the first set of MMIs is assumed to be compensated with the phase shifters.

TABLE I: On-Chip Loss per Wavelength

Wavelength	1310 nm	1550 nm
Grating Coupler	-2.5 dB	-3.5 dB
Waveguide (total)	-0.3 dB	-0.3 dB
MMI Network (ideal)	-6.0 dB	-6.0 dB
MMI Network (additional)	-3.8 ± 0.3 dB	-3 ± 0.3 dB
Total loss per output port	-12.6 ± 0.3 dB	-12.8 ± 0.3 dB

B. Electrical Output Stage

The schematic for the electrical output stage per channel is given in Fig. 1b. It features a differential input stage, variable gain amplifiers, 50 Ω output buffers, and a direct current offset cancellation. While an automatic gain control is also implemented, the manual gain was used throughout the later experiments. Further information on the circuit design may be found in [21]. The power consumption of the output stage is 450 mW. For the total power consumption of the receiver, an additional approximately 10 mW for the phase shifter in the optical circuit needs to be included.

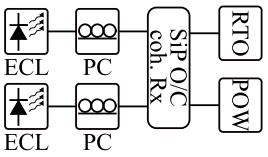

Fig. 3: Heterodyne bandwidth measurement setup. ECL: external-cavity laser, PC: polarization controller, RTO: real-time oscilloscope, POW: electrical power meter.

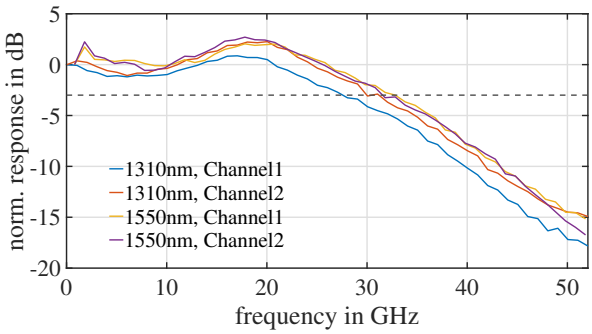

Fig. 4: Measured opto-electrical response of the dual window coherent receiver. Results are shown for channel 1 and 2 for 1310 nm and 1550 nm.

III. Experimental Setup

The receiver is probed and evaluated on wafer-level using RF- and DC-probes and a 4 channel fiber array is used for optical coupling. The coupling angle is optimized for 1310 nm, since the O-band will suffer from additional penalties in the system experiment due to the available equipment, as will be explained in Section III-B. While the receiver supplies differential output channels, measurements were done using single-ended signals due to limitations in the available equipment.

A. Receiver Bandwidth

The opto-electrical bandwidth is determined using the heterodyne setup shown in Fig. 3. Two continuous wave external cavity lasers (ECLs), either for the O- or C-band, are mixed on the dual window receiver at 2 V reverse photodiode bias voltage. One of the lasers is then remotely swept and the beating is measured using an electrical power meter (Rohde&Schwarz NRP-Z57). The systematic offset between the two lasers is measured at 1550 nm and 1310 nm using a real-time oscilloscope (RTO, Tektronix DPO77002SX). Frequency responses of the RF probe and cables are de-embedded. Results for the measured frequency characteristic are shown in Fig. 4, both for channel 1 and 2 (compare Fig. 1a), at 1310 nm and 1550 nm. The 3 dB bandwidth is mostly > 30 GHz, with channel 1 being slightly below that for 1310 nm. The difference in bandwidth at 1310 nm for channel 1 is presumably caused by variations in the photodiode response and electrical mismatch during the

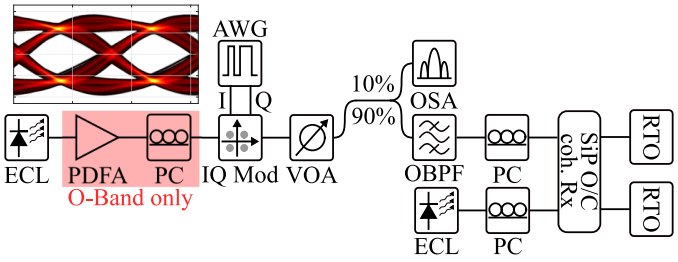

Fig. 5: Intradyne transmission setup. The inset shows an electrical eye diagram at 64 GBd supplied by the AWG (re-sampled). ECL: external-cavity laser, PDFA: praseodymium-doped fiber amplifier, PC: polarization controller, IQ Mod: IQ modulator, AWG: arbitrary waveform generator, VOA: variable optical attenuator, OSA: optical spectrum analyzer, OBPF: optical bandpass filter, RTO: real-time oscilloscope.

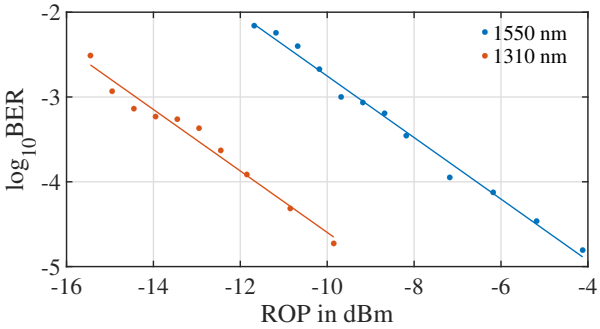

Fig. 6: Measured BER at varied ROPs at 64 GBd QPSK for 1550 nm and 1310 nm using the dual window coherent receiver. A linear regression is fit to the measured BERs. Local oscillator power at 1310 nm and 1550 nm is approximately +5.7 dBm and +11 dBm, respectively to maintain a similar photocurrent for both wavelengths.

measurement, owing to the cable connection being disassembled and reconnected to measure the different channels at both wavelengths.

B. 64 GBd QPSK Experiment

The receiver performance on a system-level is evaluated using an intradyne back-to-back setup, as depicted in Fig. 5. With minimal changes, the same setup is used for both, 1310 nm and 1550 nm. Due to the present unavailability of dedicated coherent O-band equipment, a commercial $LiNbO_3$ C-band IQ modulator (ID Photonics OMFT) is used for 1310 nm as well. Presently, this leads to additional loss, imbalance, and phase error. While ECLs are used for signal and local oscillator (LO) in both optical bands, at 1310 nm, the signal is pre-amplified using a praseodymium-doped fiber amplifier (PDFA, FiberLabs AMP-FL5601-OB) to maintain an identical signal strength in front of the modulator. This is necessary due to the limited output power of the available O-band laser. The electrical 64 GBd QPSK signals are supplied by an arbitrary waveform generator (AWG, Keysight 8199A, 256 GSa/s), with an electrical eye shown as inset in Fig. 5. Root-raised-cosine (RRC) pulse-shaping with a roll-off factor of 0.4 is used to limit the bandwidth. Subsequent to the modulation, a VOA (Keysight N7752A) is implemented to adjust the received optical power (ROP) during the experiment. Varied ROPs are used in this experiment instead of variations of the optical signal-to-noise ratio, since a potential application for O- and C-band coherent receiver also entails emerging data center applications [6], which would be ROP limited.

The modulated signal is fed through a 10 dB splitter, with the 10% portion of the signal connected to an optical spectrum analyzer for monitoring. The 90% portion is connected to an optical bandpass filter (OBPF) with 1 nm bandwidth, to remove any undesired amplified spontaneous emission noise from the PDFA in the O-band measurement. For consistency, an OBPF is also used at 1550 nm, though no optical amplifier was used. Signal and LO are then coupled into the dual window coherent receiver, with LO powers of approximately +5.7 dBm and +11 dBm for 1310 nm and 1550 nm, respectively. The reasoning behind different LO powers is as follows. Presently, at identical power levels, O- and C-Band LOs (and signals) do not generate an identical photo current. With the C-band photo current being smaller at the same power, signal power and LO power will need to be raised compared to the O-band values to achieve a similar performance. Therefore, the C-band LO power is increased. This deviation is presumably caused by: 1) Different coupling efficiencies for O- and C-band GRCs and losses of the MMI network (compare Table I). 2) Process tolerances may also lead to varying photo currents between 1310 nm and 1550 nm. By using different LO powers, this is effect is only mitigated for the LO. Any differences in bit error rate (BER) measured during the experiment are then solely due to the received signal quality, i.e., the photo current generated by the received signal. The receiver outputs are connected to two real-time oscilloscopes (Tektronix DPO77002SX, 200 GSa/s, bandwidth limited to 40 GHz). For offline digital signal processing (DSP) and BER measurement, a commercial analyzer tool (Tektronix OM1106) is used. The DSP operations include clock recovery, phase estimation, RRC filtering and least-mean-square equalization based on the symbol decision and the constant modulus algorithm. The DSP is identical for O- and C-band operation.

Measured BERs over varied ROPs for 64 GBd QPSK are shown in Fig. 6, and respective eye diagrams and constellations for 1310 nm and 1550 nm in Fig. 7. Both BER curves also feature a linear fit, yielding a similar gradient. Using identical input powers at the modulator, the ROP for 1310 nm is approximately 5.5 dB lower than for the C-band, which is due to the aforementioned additional loss of the IQ modulator in the O-band. However, this difference is very close to the difference in LO power, which is 5.3 dB, chosen to compensate for the different photo currents at both wavelengths in the LO paths. Therefore, the 5.5 dB higher received signal power in the C-band generates a similar photo current to the O-band signal. This effect can be seen in Fig. 6. At the respectively highest ROP in the O-band (-9.9 dBm) and C-band (-4.2 dBm), a similar photo current is generated and a likewise similar BER measured, despite the difference in ROP. With both, signal and

TABLE II: Comparison of Recent Integrated Silicon Photonic Coherent Receiver

Metric	Ref. 22	Ref. 11	Ref. 12	Ref. 23	This work
Technology	IMEC iSiPP25G PIC + 0.13 μm BiCMOS IC	IHP SG25H4_EPIC	IHP SG25H5_EPIC	Global Foundries 45RF-SOI 45 nm CMOS IC + 9WG 90 nm PIC	IHP SG25H5_EPIC
Degree of Integration	hybrid	monolithic	monolithic	hybrid	monolithic
Optical Band	C-band	C-band	O-band	O-band	O- and C-band
Opto-Electrical Bandwidth (3dB)	30 GHz	34 GHz	30 GHz [10]	23 GHz (simulated)	28-33 GHz
Footprint	0.2 mm^2 (PIC), n.a. (EIC)	2.75 mm^2	5.3 mm^2	6.6 mm^2 (PIC), 2.4 mm^2 (EIC)	6 mm^2
Modulation Format	QPSK, QAM-16	QPSK	QPSK	QPSK	QPSK
Symbol Rate	40 GBd	64 GBd	56 GBd	50 GBd	64 GBd
Bit Rate	80 Gb/s (QPSK), 160 Gb/s (QAM-16)	128 Gb/s	112 Gb/s	100 Gb/s	128 Gb/s
Power Consumption	310 mW	416 mW	485 mW	98 mW	460 mW
Power Consumption per Bit	3.9 pJ/bit (QPSK), 1.9 pJ/bit (QAM-16)	3.3 pJ/bit	4.3 pJ/bit	0.98 pJ/bit	3.6 pJ/bit

LO, being around 5 dB stronger in the C-band, the difference in generated photo current is compensated and an analogous BER performance achieved.

Table II compares the device presented in this work to other recently published silicon photonic coherent receiver. The devices in [22] and [23] are hybrid photonic integrated circuits (PIC) with either 0.13 μm BiCMOS [22] or 45 nm CMOS [23] electronic integrated circuits (EIC). Please note, that the previous work on multiband coherent receiver [13] has been excluded from this list, as insufficient information was available on the device. A factor that should be considered is a potentially increased footprint due to the more complex MMI network, and reported chip areas are also shown in Table II, if available. The dimensions of the receiver in this work are chiefly governed by the electrical circuit and the vertical fiber array coupling. Of the 6 mm^2 footprint, around 30% account for area reserved for the fiber array. In that regard, the MMI network has no impact on the overall device footprint. For an adequate comparison to the other works in Table II, one needs to consider that the chip area can vary greatly, based on the coupling scheme and integration approach. In hybrid integrated devices both, the PIC and EIC footprints, need to be considered when compared to fully monolithic devices. Noteworthy is the O-band coherent receiver in [23], as it is the only device in this list supporting edge-coupling. The receiver reported in that work is a hybrid integration of 45 nm CMOS electronics and 90 nm PIC, which results in a very low power consumption of approximately 1 pJ/bit, though bandwidth and symbol rate are limited. Despite the trade-off of optimizing the MMI network at 1430 nm, the coherent receiver demonstrated in this work achieves state-of-the-art performance at 64 GBd, which is the highest yet reported symbol rate for an O-band coherent link. In contrast to the previously reported devices in Table II, the receiver in this contribution also enables coherent communication in multiple optical bands.

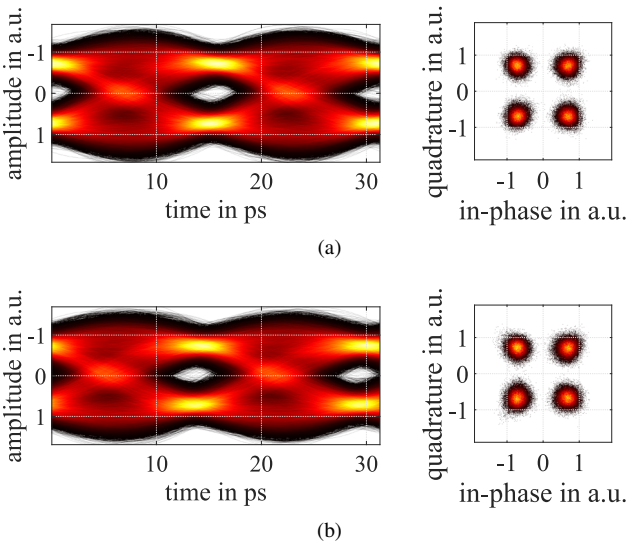

Fig. 7: Recovered eye diagrams and constellations for a) 1550 nm, ROP = -4.2 dBm b) 1310 nm, ROP = -9.9 dBm at 64 GBd QPSK. The eye diagrams have been resampled. The data are color-coded to an absolute bin count.

IV. Conclusion

The dual window coherent receiver presented in this work has been characterized at 64 GBd QPSK, resulting in BERs as low as 1.563 $\cdot 10^{-5}$ at 1550 nm. The demonstrated performance is on a par with present record BiCMOS coherent receiver for the C-band [11]. However, the device presented in this work enables coherent communication not only in the C-band, but the O-band as well. Further improvements are possible by extending this approach towards coherent multi-level formats, e.g. quadrature amplitude modulation (QAM)-16. At 1310 nm, a low power LO of approximately +5.7 dBm has been used, which is advantageous in potential data center applications, where power consumption is a prime resource.

In the C-band, the LO power was raised to approximately +11 dBm, to compensate for differences in coupling efficiency and process variation, i.e. the external photodiode responsivity. Since higher LO powers are desirable in long-haul C-band applications, the extra expense in power consumption is reasonable. In the future, an optimized design using spot-size converters should be used, which not only improves the coupling efficiency in O- and C-band, but also opens the device to applications in E- and S-band, as the 2 $\times$2 MMI network is designed with a central wavelength of 1430 nm. Additionally, the broadband operation of the receiver could be further optimized, as the 2 $\times$ 2 MMIs in this work already show a reduced performance at 1310 nm and 1550 nm, with excess loss greater 1.5 dB per coupler and phase errors around 10°. Promising results for ultra-broadband MMIs featuring sub-wavelength gratings with excess loss and imbalance below 1 dB, and a phase error below 5° over a bandwidth greater than 300 nm have been demonstrated [24]. To the best of our knowledge, this is the first demonstration of a monolithically integrated silicon photonic coherent receiver for multiband communication achieving 64 GBd performance.

ACKNOWLEDGMENT

This work was supported in part by the German Research Foundation (DFG) through the projects ULTRA (ZI 1283-5-1), EPIC-Sense (ZI 1283-6-1), and EPIDAC (ZI 1283-7-1), by the Federal Ministry of Education and Research (BMBF) through project PEARLS (13N14936), and the European Commission through project H2020-SPACE-ORIONAS (822002).

REFERENCES

[1] A. Feldmann, O. Gasser, F. Lichtblau, E. Pujol, I. Poese, C. Dietzel, D. Wagner, M. Wichtlhuber, J. Tapiador, N. Vallina-Rodriguez, O. Hohlfeld, and G. Smaragdakis, "The Lockdown Effect: Implications of the COVID-19 Pandemic on Internet Traffic," in *Internet Meas. Conf. (IMC) 2020*. Pittsburgh, Pennsylvania, USA, Oct. 2020.

[2] X. Zhou, R. Urata, and H. Liu, "Beyond 1Tb/s datacenter interconnect technology: Challenges and solutions (Invited)," in *Opt. Fiber Commun. Conf. (OFC) 2019*. San Diego, California, United States, 2019.

[3] R. Urata, H. Liu, X. Zhou, and A. Vahdat, "Datacenter interconnect and networking: from evolution to holistic revolution," in *2017 Opt. Fiber Commun. Conf. and Exhib. (OFC)*. Los Angeles, California, United States, 2017, pp. 1–3.

[4] M. H. Eiselt, A. Dochhan, and J.-P. Elbers, "Data center interconnects at 400G and beyond," in *2018 23rd Opto-Electron. Commun. Conf. (OECC)*. Jeju, Korea (South), Jul. 2018.

[5] E. Maniloff, S. Gareau, and M. Moyer, "400G and beyond: Coherent evolution to high-capacity inter data center links," in *Opt. Fiber Commun. Conf. (OFC) 2019*. San Diego, California, United States, 2019.

[6] P. M. Seiler, G. Georgieva, G. Winzer, A. Peczek, K. Voigt, S. Lischke, A. Fatemi, and L. Zimmermann, "Toward coherent O-band data center interconnects," *Front. Optoelectron.*, vol. 14, no. 4, pp. 414–425, Dec. 2021.

[7] R. Emmerich, M. R. Sena, R. Elschner, C. Schmidt-Langhorst, I. Sackey, C. Schubert, and R. Freund, "Enabling S-C-L-Band Systems with Standard C-Band Modulator and Coherent Receiver using Coherent System Identification and Nonlinear Predistortion," *J. Lightw. Technol.*, pp. 1–1, 2021.

[8] S. Sun, M. He, M. Xu, S. Gao, S. Yu, and X. Cai, "Hybrid silicon and lithium niobate modulator," *IEEE J. Sel. Top. Quantum Electron*, vol. 27, no. 3, pp. 1–12, may 2021.

[9] G. Ronniger, I. Sackey, T. Kernetzky, U. Höfler, C. Mai, C. Schubert, N. Hanik, L. Zimmermann, R. Freund, and K. Petermann, "Efficient Ultra-Broadband C-to-O Band Converter Based on Multi-Mode Silicon-on-Insulator Waveguides," in *2021 Eur. Conf. Opt. Commun. (ECOC), We1G.1*. Bordeaux, France, 2021.

[10] P. M. Seiler, K. Voigt, S. Lischke, A. Malignaggi, and L. Zimmermann, "Ultra-Wideband Silicon Photonic BiCMOS Coherent Receiver for O- and C-Band," in *2021 Eur. Conf. Opt. Commun. (ECOC) Postdeadline Papers*. Bordeaux, France, sep 2021.

[11] S. Gudyriev, C. Kress, H. Zwickel, J. N. Kemal, S. Lischke, L. Zimmermann, C. Koos, and J. C. Scheytt, "Coherent ePIC Receiver for 64 GBaud QPSK in 0.25 μm Photonic BiCMOS Technology," *J. Lightw. Technol.*, vol. 37, no. 1, pp. 103–109, Jan. 2019.

[12] P. M. Seiler, A. Peczek, G. Winzer, K. Voigt, S. Lischke, A. Fatemi, and L. Zimmermann, "56 GBaud O-Band Transmission using a Photonic BiCMOS Coherent Receiver," in *2020 Eur. Conf. Opt. Commun. (ECOC)*. Brussels, Belgium, 2020.

[13] C. Doerr, L. Chen, T. Nielsen, R. Aroca, L. Chen, M. Banaee, S. Azemati, G. McBrien, S. Y. Park, J. Geyer, B. Guan, B. Mikkelsen, C. Rasmussen, M. Givehchi, Z. Wang, B. Potsaid, H. C. Lee, E. Swanson, and J. G. Fujimoto, "O, E, S, C, and L Band Silicon Photonics Coherent Modulator/Receiver," in *Opt. Fiber Commun. Conf. Exhib. (OFC)*. Anaheim, California, United States, 2016.

[14] D. Knoll, S. Lischke, R. Barth, L. Zimmermann, B. Heinemann, H. Rücker, C. Mai, M. Kroh, A. Peczek, A. Awny, C. Ulusoy, A. Trusch, A. Kruger, J. Drews, M. Fraschke, D. Schmidt, M. Lisker, K. Voigt, E. Krune, and A. Mai, "High-performance photonic BiCMOS process for the fabrication of high-bandwidth electronic-photonic integrated circuits," in *2015 IEEE Intl. Electron Devices Meeting (IEDM)*. Washington, DC, USA, Dec. 2015.

[15] S. Lischke, D. Knoll, C. Mai, and L. Zimmermann, "Advanced photonic BiCMOS technology with high-performance Ge photo detectors," in *Proc. SPIE 11088, Optical Sensing, Imaging, and Photon Counting: From X-Rays to THz 2019*, O. Mitrofanov, Ed. SPIE, Sep. 2019.

[16] R. Kunkel, H.-G. Bach, D. Hoffmann, C. Weinert, I. Molina-Fernandez, and R. Halir, "First monolithic InP-based 90°-hybrid OEIC comprising balanced detectors for 100GE coherent frontends," in *2009 IEEE Intl. Conf. Indium Phosphide Relat. Mater.* Newport Beach, CA, USA, May 2009.

[17] Y. Sakamaki, Y. Nasu, T. Hashimoto, K. Hattori, T. Saida, and H. Takahashi, "Reduction of phase-difference deviation in 90° optical hybrid over wide wavelength range," *IEICE Electron. Express*, vol. 7, no. 3, pp. 216–221, 2010.

[18] K. Voigt, L. Zimmermann, G. Winzer, and K. Petermann, "SOI based 2 $\times$ 2 and 4 $\times$ 4 waveguide couplers - evolution from DPSK to DQPSK," in *2008 5th IEEE Int. Conf. on Group IV Photonics*. Sorrento, Italy, 2008.

[19] G. Georgieva, P. M. Seiler, C. Mai, K. Petermann, and L. Zimmermann, "2D Grating Coupler Induced Polarization Crosstalk in Coherent Transceivers for Next Generation Data Center Interconnects," in *Opt. Fiber Commun. Conf. (OFC) 2021*. Washington, DC, United States, Jun. 2021.

[20] S. Lischke, D. Knoll, C. Mai, and L. Zimmermann, "High-performance waveguide-coupled Ge photo detectors for a photonic BiCMOS Technology," in *2018 23rd Opto-Electron. Commun. Conf. (OECC)*. Jeju, Korea (South), Jul. 2018.

[21] G. Dziallas, A. Fatemi, A. Peczek, L. Zimmermann, A. Malignaggi, and G. Kahmen, "A 56-Gb/s Optical Receiver With 2.08-μA Noise Monolithically Integrated into a 250-nm SiGe BiCMOS Technology," *IEEE Trans. Microw. Theory Tech.*, pp. 1–1, Aug. 2021.

[22] J. Verbist, J. Zhang, B. Moeneclaey, W. Soenen, J. V. Weerdenburg, R. V. Uden, C. Okonkwo, J. Bauwelinck, G. Roelkens, and X. Yin, "A 40-GBd QPSK/16-QAM Integrated Silicon Coherent Receiver," *IEEE Photon. Technol. Lett.*, vol. 28, no. 19, pp. 2070–2073, Oct. 2016.

[23] H. Andrade, Y. Xia, A. Maharry, L. Valenzuela, J. Buckwalter, and C. Schow, "50 GBaud QPSK 0.98 pJ/bit receiver in 45 nm CMOS and 90 nm silicon photonics," in *2021 Eur. Conf. Opt. Commun. (ECOC)*. Bordeaux, France, Sep. 2021.

[24] R. Halir, P. Cheben, J. M. Luque-González, J. D. Sarmiento-Merenguel, J. H. Schmid, G. Wangüemert-Pérez, D.-X. Xu, S. Wang, A. Ortega-Moñux, and Í. Molina-Fernández, "Ultra-broadband nanophotonic beamsplitter using an anisotropic sub-wavelength metamaterial," *Laser & Photonics Reviews*, vol. 10, no. 6, pp. 1039–1046, Nov 2016.